Interband absorption in quantum wires. I. Zero-magnetic-field case

U. Bockelmann
Laboratoire de Physique de la Matière Condensée de l'Ecole Normale Supérieure, 24 rue Lhomond, F-75005 Paris, France and Walter Schottky Institut der TU München, Am Coulombwall, D-8046 Garching, Germany

G. Bastard
Laboratoire de Physique de la Matière Condensée de l'Ecole Normale Supérieure, 24 rue Lhomond, F-75005 Paris, France
(Received 13 March 1991)

We describe the theory of interband transitions in quasi-one-dimensional semiconductor structures. It is based on the effective-mass approximation and takes into account the mixing of the heavy-hole and the light-hole states in the valence band. The dipole matrix element for optical transitions between the valence-band and the conduction-band states is derived for different linear photon polarizations with respect to the wire orientation. The theory is applied to single wires and periodic arrays of coupled wires exhibiting spatially direct or indirect optical transitions. We also study the influence of sample imperfections by calculating the optical properties of a statistical ensemble of confinement potentials exhibiting random fluctuations.

I. INTRODUCTION

In quasi-one-dimensional (1D) structures as will be discussed in this paper the semiconductor crystal periodicity is maintained in only one spatial direction. Perpendicular to it, artificially introduced potentials modify the probability densities of the carriers on a nanometer length scale. Due to progresses in the epitaxial growth of III-V semiconductor layers and in nanostructuring techniques, such 1D systems are becoming realizable with increasing quality, nowadays.[1]

The spectroscopy of optical transitions across the band gap (interband transitions) is a powerful and versatile method to study the electronic structure of semiconductors. Such experimental activities are increasing in 1D structures. Some effects, which were related to a 1D carrier motion, have already been observed in photoluminescence and photoluminescence-excitation spectra,[2–8] and their dependence on the light polarization[6–8] and on time[9] has been studied. Recently, single-particle and collective excitations of the 1D electron gas have been investigated by Raman spectroscopy.[10,11]

On the theoretical side, there have already been some calculations of the energy levels in the conduction and valence bands of 1D structures.[12–15] Until recently, 1D interband transitions have been studied only in the parabolic approximation for the valence band.[16–18] A proper treatment of the valence band leads not only to modified transition energies and oscillator strengths, but is necessary to account for the different possible polarizations of the light relative to the wire structure. The absorption of a light beam traveling parallel to the epitaxial growth axis is more easily measurable than that of a beam traveling perpendicular to it. Recently, we have shown[19] that the polarization dependence of the absorption in the former configuration is determined by the heavy-hole (hh) or light-hole (lh) character and the amount of hh-lh mixing of the 1D valence subbands.

In the present paper we develop the theory of the polarization-dependent interband absorption by 1D structures in detail and present results for different confinement potentials. It is organized as follows. Section II contains the theoretical framework. We define the relevant absorption quantities (Sec. II A), show how the 1D eigenstates are calculated (Sec. II B) and develop the expression for the polarization dependence of the interband matrix element (Sec. II C). In Sec. III the theory is applied to different 1D structures. In Sec. IV we investigate the influence of statistical fluctuations of the confining potential. In Sec. V we finally discuss the limitations and the applicability of our theoretical results to actual experimental situations. The influence of a magnetic field on the optical properties of 1D structures will be studied in the following paper [U. Bockelmann and G. Bastard, Phys. Rev. B **45**, 1700 (1992)].

II. THEORETICAL BASIS

A. Derivation of the absorption quantities

In general, the electronic structure and the dielectric properties of lower-dimensional systems can be modified in comparison with those of the 3D crystal. We are interested in how the electronic structure finds expression in the optical properties of 1D systems. It is assumed that the refractive index n is spatially constant. This should work fine for a light wave propagating in as-grown or overgrown etched quantum wires that are based on semiconductor heterostructures with similar refractive indices of the host materials (e.g., GaAs-AlAs). In free-standing etched structures the spatial variation of n may be of importance. Variations of n, caused by the absorption to be calculated, are negligible in real systems where any singularity of the joint density of states is suppressed

by level broadening.

In the dipole approximation, the absorption coefficient α for a plane electromagnetic wave in a medium of refractive index n is given[20,21] by

$$\alpha=\frac{\pi e^2}{nc\epsilon_0 m_0^2\omega V}\sum_{i,f}|\langle f|\boldsymbol{\epsilon}\cdot\mathbf{p}|i\rangle|^2\delta(E_f-E_i-\hbar\omega)\ . \tag{1}$$

ϵ_0, m_0, V, and $\hbar\omega$ represent the permitivity of free space, the mass of the free electron, the sample volume, and the photon energy, respectively. The polarization vector $\boldsymbol{\epsilon}$ defines the orientation of the electric field of the linearly polarized wave. It is assumed that any initial electronic state i (final state f) is occupied (unoccupied).

In 0D, 1D, and 2D systems the sample volume V has to be replaced by 1, $\mathcal{L}_y$ (length of the wire), and $\mathcal{L}_x\mathcal{L}_y$ (area of the 2D layer), respectively, in order to obtain an unambiguous definition of an absorption quantity via Eq. (1). This can be seen by converting the sum into integrals $(\mathcal{L}_\nu/2\pi\int dk_\nu)$ for the directions ν that are translationally invariant. In the other spatial directions ill-defined lengths remain in the expression of α. The proposed replacements of V in Eq. (1) avoid this problem by absorbing these lengths in the definitions of the absorption quantities: 3D—α, in units of m^{-1}; 2D—$\alpha\mathcal{L}_z$, in units of 1; 1D—$\alpha\mathcal{L}_x\mathcal{L}_z$, in units of m; 0D—$\alpha\mathcal{L}_x\mathcal{L}_y\mathcal{L}_z$, in units of m^2. In a way, the definitions of an "effective wire width" $\alpha\mathcal{L}_x\mathcal{L}_z$ for 1D systems and an "absorption probability" $\alpha\mathcal{L}_z$ for 2D systems close the gap between the absorption cross section $\sigma_{\mathrm{abs}}=\alpha\mathcal{L}_x\mathcal{L}_y\mathcal{L}_z$ and the absorption coefficient α, which are well known from atomic and solid-state physics. In Appendix A, these definitions are explicitly related to the attenuation of a light wave that propagates parallel or perpendicular to 1D or 2D structures.

B. One-dimensional conduction- and valence-band states

In order to calculate interband transitions, the energy dispersions and wave functions of the initial and the final electron states have to be known. This paper deals with the optical transitions that are close in energy to the fundamental absorption across the bulk semiconductor band gap. We suppose that the initial and final electron states are eigenstates separately described by the valence band Γ_8 and the conduction band Γ_6 effective-mass Hamiltonians, respectively. In that way, we neglect the presence of the electron-hole Coulomb interaction (excitonic effects) and suppose that the band-gap energy as well as the splitoff energy are sufficiently large to prevent a sizeable coupling between the Γ_6, Γ_7, and Γ_8 bands. As usual, the lower-dimensional electronic states are built on these bulk bands in the envelope-function approximation.[21]

The conduction-band (Γ_6) wave functions are written as

$$\Psi^c_{m_s}(\mathbf{r})=f^c(\mathbf{r})u^c_{m_s}(\mathbf{r})\ , \tag{2}$$

where the $u^c_{m_s}(\mathbf{r})$ are the two spin-degenerate ($s=\frac{1}{2}, m_s=\pm\frac{1}{2}$) Bloch functions at the bottom of the Γ_6 bulk band ($\mathbf{k}=\mathbf{0}$).

In the valence band (Γ_8), we have to account for two different carrier types, which originate from the $\mathbf{k}=\mathbf{0}$ degenerate heavy-hole and light-hole bands of the bulk semiconductor. There, the equivalent of Eq. (2) reads

$$\Psi^v(\mathbf{r})=\sum_{m_j} f^v_{m_j}(\mathbf{r})u^v_{m_j}(\mathbf{r})\ . \tag{3}$$

The $u^v_{m_j}(\mathbf{r})$ are the degenerate Bloch functions at the top of the Γ_8 bulk bands. The sum extends over the four expectation values ($m_j=\pm\frac{3}{2}$ for the hh and $\pm\frac{1}{2}$ for the lh) of the $j=\frac{3}{2}$ multiplet.

For the sake of simplicity we assume that the potential $W(x,z)$ that confines the carriers into the 1D structure can be written as $W(x,z)=V_x(x)+V_z(z)$. In addition, any dependence of the effective mass in a given direction on the motion perpendicular to it is neglected. According to that, the envelope wave functions in Eqs. (2) and (3) separate in the three spatial coordinates x, y, and z. This "decoupling approximation" describes well the common situation, where the confinement in the growth direction (z) is stronger than that in the lateral direction (x).[12]

In the conduction band, the envelope wave function

$$f^c(\mathbf{r})=\varphi_e(x)\mathcal{L}_y^{-1/2}e^{ik_y y}\chi_e(z)$$

and the corresponding energy $E=E_{xy}+E_z$ are determined by the following two differential equations:

$$\left[\frac{\hbar^2}{2m^*(0)}(-\partial_x^2+k_y^2)+V_x(x)-E_{xy}\right]\varphi_e(x)=0\ , \tag{4a}$$

$$\left[-\frac{\hbar^2}{2}\partial_z\frac{1}{m^*(z)}\partial_z+V_z(z)-E_z\right]\chi_e(x)=0\ . \tag{4b}$$

$m^*(z)$ is the (z-dependent) effective mass at the bottom of the Γ_6 band and k_y is the carrier wave vector of the in-wire motion.

The calculation of the Γ_8 valence band starts from the Hamiltonian:

$$H_{\Gamma_8}=\begin{vmatrix} H_{\mathrm{hh}} & c & b & 0\\ c^+ & H_{\mathrm{lh}} & 0 & -b\\ b^+ & 0 & H_{\mathrm{lh}} & c\\ 0 & -b^+ & c^+ & H_{\mathrm{hh}}\end{vmatrix}\begin{vmatrix}\frac{3}{2}\\ -\frac{1}{2}\\ \frac{1}{2}\\ -\frac{3}{2}\end{vmatrix}\ , \tag{5}$$

where

$$H_{\mathrm{hh}}=\frac{\hbar^2}{2m_0}[(\gamma_1+\gamma_2)(\partial_x^2-k_y^2)+\partial_z(\gamma_1-2\gamma_2)\partial_z]+V_x(x)+V_z(z)\ , \tag{6}$$

$$H_{\mathrm{lh}}=\frac{\hbar^2}{2m_0}[(\gamma_1-\gamma_2)(\partial_x^2-k_y^2)+\partial_z(\gamma_1+2\gamma_2)\partial_z]+V_x(x)+V_z(z)\ , \tag{7}$$

$$b=-\frac{\hbar^2\sqrt{3}}{2m_0}(\partial_x+k_y)(\gamma_3\partial_z+\partial_z\gamma_3)\ , \tag{8}$$

$$c=-\frac{\hbar^2\sqrt{3}}{2m_0}\frac{\gamma_2+\gamma_3}{2}(\partial_x+k_y)^2 \ . \tag{9}$$

Equation (5) has been derived from the original work of Luttinger and Kohn (Eq. V.13 of Ref. 22) by replacing k_x by $-i\partial_z$, k_z by $-i\partial_z$, and by symmetrizing any product of noncommuting factors. The phases of the periodic wave functions $u^v_{m_j}(\mathbf{r})$ are changed with respect to Ref. 22 in order to obtain a real H_{Γ_8}. We use

$$\begin{aligned}
u^v_{3/2}&=2^{-1/2}|(x+iy)\uparrow\rangle \ ,\\
u^v_{-1/2}&=-6^{-1/2}|(x-iy)\uparrow\rangle-(\tfrac{2}{3})^{1/2}|z\downarrow\rangle \ ,\\
u^v_{1/2}&=6^{-1/2}|(x+iy)\downarrow\rangle-(\tfrac{2}{3})^{1/2}|z\uparrow\rangle \ ,\\
u^v_{-3/2}&=-2^{-1/2}|(x-iy)\downarrow\rangle \ ,\\
u^c_{1/2}&=i|s\uparrow\rangle \ ,\\
u^c_{-1/2}&=i|s\downarrow\rangle \ .
\end{aligned} \tag{10}$$

The Luttinger parameters γ_1-γ_3 describe the coupling between the Γ_8 and the edges of all the other host bands[23] and are in principle z dependent. In Eq. (9) the matrix element c is given in the axial approximation.[24]

If $V_z(z)$ and the γ's are even functions of z, the envelope functions can be chosen to have a definite parity in the z direction. The off-diagonal elements of H_{Γ_8} couple functions of either opposite (b,b^+) or equal (c,c^+) parity. This implies that there are two decoupled types of Γ_8 wave functions: $\Psi\uparrow$ and $\Psi\downarrow$. The first (second) exhibit even, even, odd, odd (odd, odd, even, even) z parity of their envelope functions $f^v_{3/2},f^v_{-1/2},f^v_{1/2},f^v_{-3/2}$, respectively. The notations $\Psi\uparrow$ and $\Psi\downarrow$ point out that the corresponding energy levels are degenerate at zero magnetic field B, while they split for nonzero B.

Our calculations presented in Secs. III and IV suppose a symmetric GaAs-$Ga_{0.7}Al_{0.3}As$ quantum well in the z direction that gives rise to a relatively large subband separation with respect to the energy range of interest (stronger confinement in z than in x). Then we can restrict the expansion to the three lower band edge eigenstates of that quantum well: the first hh, the first lh, and the second hh states ($\chi_{\rm hh1}$, $\chi_{\rm lh1}$, and $\chi_{\rm hh2}$), respectively.[25] This approximation leads to the following Γ_8 wave functions:

$$\begin{aligned}
\Psi^v_\uparrow=[&\varphi^\uparrow_{\rm hh1}(x)\chi_{\rm hh1}(z)(z)u^v_{3/2}+\varphi^\uparrow_{\rm lh1}(x)\chi_{\rm lh1}(z)u^v_{-1/2}\\
&+\varphi^\uparrow_{\rm hh2}(x)\chi_{\rm hh2}(z)u^v_{-3/2}]\mathcal{L}_y^{-1/2}e^{ik_yy} \ ,
\end{aligned} \tag{11a}$$

$$\begin{aligned}
\Psi^v_\downarrow=[&\varphi^\downarrow_{\rm hh1}(x)\chi_{\rm hh1}(z)u^v_{-3/2}+\varphi^\downarrow_{\rm lh1}(x)\chi_{\rm lh1}(z)u^v_{1/2}\\
&+\varphi^\downarrow_{\rm hh2}(x)\chi_{\rm hh2}(z)u^v_{3/2}]\mathcal{L}_y^{-1/2}e^{ik_yy} \ .
\end{aligned} \tag{11b}$$

By applying H_{Γ_8} on Eq. (11a) we obtain a system of three coupled eigenvalue equations for the envelope functions $\varphi^\uparrow_{\rm hh1}$, $\varphi^\uparrow_{\rm lh1}$, and $\varphi^\uparrow_{\rm hh2}$ and the eigenenergy E:

$$(\mathcal{H}-E1)[\varphi^\uparrow_{\rm hh1}(x),\varphi^\uparrow_{\rm lh1}(x),\varphi^\uparrow_{\rm hh2}(x)]=0 \ , \tag{12}$$

where

$$\mathcal{H}=\begin{pmatrix}
E_{\rm hh1}-\frac{\hbar^2}{2m_{\rm hh}}(-\partial_x^2+k_y^2)+V_x(x) & -\frac{\hbar^2}{2\mu}(\partial_x+k_y)^2 & 0\\
-\frac{\hbar^2}{2\mu}(-\partial_x+k_y)^2 & E_{\rm lh1}-\frac{\hbar^2}{2m_{\rm lh}}(-\partial_x^2+k_y^2)+V_x(x) & \frac{\hbar^2}{m_0l_0}(\partial_x+k_y)\\
0 & \frac{\hbar^2}{m_0l_0}(-\partial_x+k_y) & E_{\rm hh2}-\frac{\hbar^2}{2m_{\rm hh}}(-\partial_x^2+k_y^2)+V_x(x)
\end{pmatrix} ,$$

$$\mu^{-1}=\frac{\sqrt{3}}{m_0}\frac{\gamma_2+\gamma_3}{2}\langle\chi_{\rm lh1}|\chi_{\rm hh1}\rangle \ ,$$

$$l_0^{-1}=\frac{\sqrt{3}}{2}\langle\chi_{\rm lh1}|\gamma_3\partial_z+\partial_z\gamma_3|\chi_{\rm hh1}\rangle \ ,$$

$$m_{\rm hh}=\frac{m_0}{\gamma_1+\gamma_2} \ , \quad m_{\rm lh}=\frac{m_0}{\gamma_1-\gamma_2} \ .$$

$E_{\rm hh1}$, $E_{\rm lh1}$, and $E_{\rm hh2}$ are the edge energies of the first hh, first lh, and second hh subbands of the quantum well in the z direction [solutions of the hh and lh equivalent of Eq. (4b)]. The equation that determines $\Psi\downarrow$ rather than $\Psi\uparrow$ is obtained by reversing the signs of all terms proportional to ∂_x and by replacing $\uparrow$ by $\downarrow$ in Eq. (12). Finally, we expand Eq. (12) in an appropriate set of basis functions (the explicit choice depends on the form of V_x) and diagonalize the resulting eigenvalue matrix numerically.

C. Polarization dependence of the interband matrix element

Since the periodic part u^c,u^v varies rapidly over the characteristic length of variation of the envelope function f^c,f^v, the dipole matrix element of a transition between a Γ_6 [Eq. (2)] and a Γ_8 [Eq. (3)] state can be written as

$$\begin{aligned}
\langle\Psi^c_{m_s}|\boldsymbol{\varepsilon}\cdot\mathbf{p}|\Psi^v\rangle&=\sum_{m_j}J_{m_j}\langle u^c_{m_s}|\boldsymbol{\varepsilon}\cdot\mathbf{p}|u^v_{m_j}\rangle \ ,\\
J_{m_j}&=\langle f^c(\mathbf{r})|f^v_{m_j}(\mathbf{r})\rangle \ .
\end{aligned} \tag{13}$$

The atomiclike dipole matrix elements give rise to the dependence on the polarization vector ε of the light wave. They are weighed by the quantum numbers of the initial and final states via the overlap integrals J_{m_j}.

The symmetry of the host functions that define the u^c, u^v by means of Eq. (10) gives rise to the selection rule

$$\langle s|p_\nu|\nu'\rangle=\delta_{\nu,\nu'}im_0P/\hbar\ ,\quad \nu,\nu'\in\{x,y,z\}\ . \tag{14}$$

For the Kane matrix element P,[20] the GaAs value $2m_0P^2=22.71$ eV is used. We express the polarization vector in spherical coordinates $\varepsilon=(\cos\varphi\sin\vartheta,\sin\varphi\sin\vartheta,\cos\vartheta)$ and evaluate Eq. (13) using Eqs. (10) and (14). We obtain

$$\sum_{m_s}|\langle\Psi^c_{m_s}|\varepsilon\cdot\mathbf{p}|\psi^v\rangle|^2=\left[\frac{m_0P}{\hbar}\right]^2\begin{cases}\frac{2}{3}(J^2_{1/2}+J^2_{-1/2}) & \text{for } \vartheta=0\\ \frac{1}{2}(J^2_{3/2}+J^2_{-3/2})+\frac{1}{6}(J^2_{1/2}+J^2_{-1/2})-\frac{1}{\sqrt{3}}(J_{3/2}J_{-1/2}+J_{1/2}J_{-3/2})\cos(2\varphi)\ , & \vartheta=\pi/2.\end{cases} \tag{15}$$

Equation (15) is very general. In particular, we have made no assumptions concerning the confining potential. Neglecting the internal anisotropy of the lattice unit cell, the absorption is independent of ε in a cubic 3D lattice. In 2D systems ($V_z\neq0$) the absorption depends on the angle ϑ. The summation over the in-plane wave vector eliminates the term proportional to $\cos(2\varphi)$ of Eq. (15). This term survives the integration over the in-wire momentum in 1D systems. The magnitude of the resulting anisotropy of the transition probability in the xy plane increases in proportion to $(J_{3/2}J_{-1/2}+J_{1/2}J_{-3/2})$ with increasing hh-lh mixing in the valence band. Let us stress that the use of decoupled hh and lh valence-band states would result in a zero xy anisotropy.

For the systems described by Eqs. (11) and (12), the polarization-dependent interband matrix element [Eq. (15)] is simply given by

$$\sum_{m_s}|\langle\psi^c_{m_s}|\varepsilon\cdot\mathbf{p}|\psi^v\rangle|^2=\left[\frac{m_0P}{\hbar}\right]^2\left[\left(J^2_{\mathrm{hh1}}+\tfrac{1}{3}J^2_{\mathrm{lh1}}-\frac{2}{\sqrt{3}}J_{\mathrm{hh1}}J_{\mathrm{lh1}}\cos(2\varphi)\right)\times\sin^2(\vartheta)+\tfrac{4}{3}J^2_{\mathrm{lh1}}\cos^2(\vartheta)\right], \tag{16}$$

where

$$J_{\mathrm{hh1}}=\int dx\ \varphi_{\mathrm{hh1}}(x)\varphi_e(x)\int dz\ \chi_{\mathrm{hh1}}(z)\chi_e(z)\ ,$$

$$J_{\mathrm{lh1}}=\int dx\ \varphi_{\mathrm{lh1}}(x)\varphi_e(x)\int dx\ \chi_{\mathrm{lh1}}(z)\chi_e(z)\ .$$

In Eq. (16) we have added the equal contributions of the two parity degenerate solutions $\Psi\uparrow$ and $\Psi\downarrow$. By χ_e we mean the ground-state wave function of Eq. (4b). χ_e and χ_{hh2} have opposite parity, hence J_{hh2} equals zero and does not appear in Eq. (16). The overlap integrals J in Eqs. (13)–(16) are supposed to be real, which is no restriction, since it is always possible to choose real solutions of the Schrödinger equation.

III. RESULTS FOR SOME 1D STRUCTURES AT ZERO MAGNETIC FIELD

In all the following 1D model systems the electrons and holes are confined in the z direction by a symmetric GaAs quantum well embedded in $Ga_{0.7}Al_{0.3}As$. We suppose that the offset of the conduction (hh and lh valence) band equals $\frac{2}{3}$ ($\frac{1}{3}$) of the band-gap difference between $Ga_{0.7}Al_{0.3}As$ and GaAs of 0.354 eV. The effective mass $m^*=0.067m_0$ ($0.083m_0$) and the Luttinger parameters $\gamma_1=6.85$ (5.83), $\gamma_2=2.10$ (1.67), $\gamma_3=2.90$ (2.42) are used for the well (barriers) throughout the calculations.

A. Infinitely deep square-well model

In a first approach we model the lateral confinement by a rectangular well of width L_x with infinite barriers for both electrons and holes. The lateral wave functions are written as

$$\varphi(x)=\sum_{n_x=1}^{\infty}c_{n_x}\sin(n_x\pi x/L_x)\ . \tag{17}$$

The basis functions $\sin(n_x\pi x/L_x)$ of this expansion are the eigenfunctions in the conduction band [Eq. (4a)]. Figure 1 demonstrates how the lateral confinement transforms the 2D valence-band dispersions of a 5-nm- (a) and a 10-nm- (b) wide quantum well into 1D subbands. The 2D branches (dashed lines) correspond at $\mathbf{k}=\mathbf{0}$ to the first hh, first lh, and second hh eigenstates [at -7, -20.5, and -27.7 meV in Fig. 1(b)]. A finite in-plane momentum $\mathbf{k}$ couples these states. In 1D systems the kinetic energy that is introduced by the lateral confinement [∂_x terms in Eqs. (8) and (9)] mixes the 2D band-edge eigenstates, even for zero in-wire wave vector k_y. Thus, any 1D valence band state has both hh and lh contributions. Nevertheless, a state with an energy in the vicinity of a 2D subband edge can display a dominant heavy- or light-hole character. Therefore the 1D and the 2D subband dispersions exhibit a similar shape in the vicinity of the 2D subband edges.

In Fig. 2 the energies at the edge of the 1D valence subbands ($k_y=0$) are plotted against the lateral width L_x of the wire. Near the 2D lh edge E_{lh1} [at -47.5 in (a) and -20.5 in (b)] the curves show a weak dependence on L_x. This is due to the flatness of the 2D lh dispersion (Fig. 1) and indicates the existence of 1D states with a strong lh contribution over the whole range of L_x. The

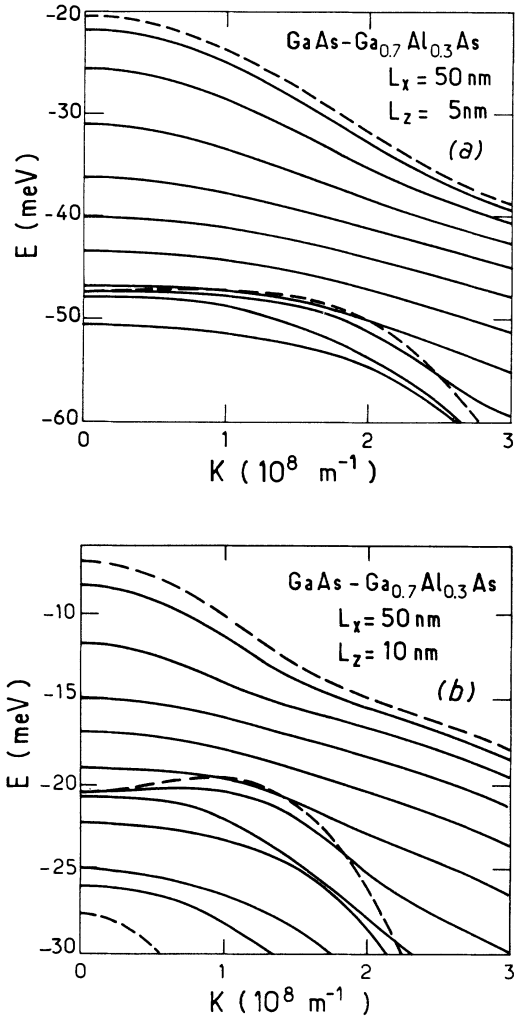

FIG. 1. Valence subbands of a quantum wire (solid lines) as a function of the in-wire wave vector and of the corresponding quantum well (dashed lines) as a function of the in-plane wave vector. The lateral wire width L_x equals 50 nm, while the well width L_z is given by (a) 5 nm or (b) 10 nm. The top of the bulk GaAs valence band corresponds to zero energy.

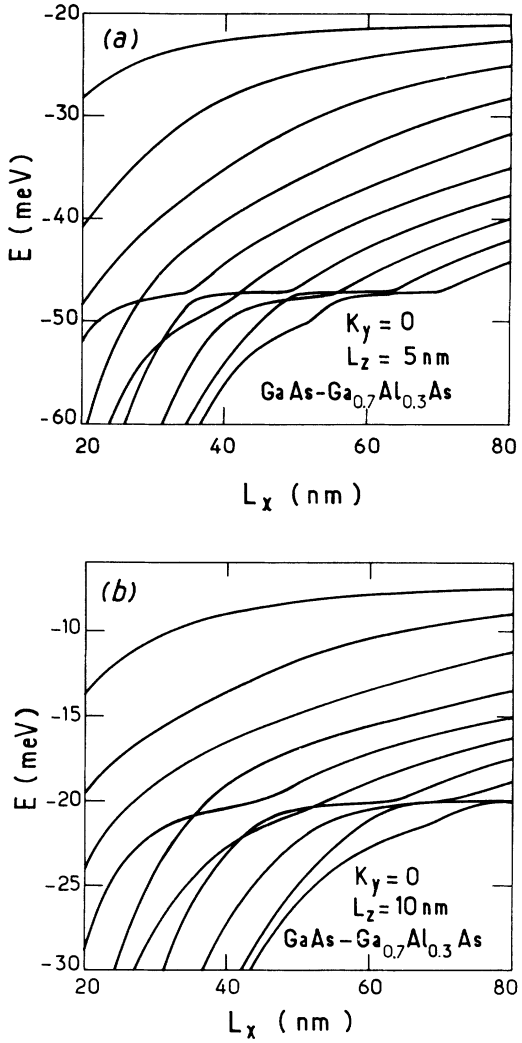

FIG. 2. Edge energies of the 1D valence subbands as a function of the lateral wire width L_x for a fixed dimension L_z of (a) 5 nm or (b) 10 nm.

curves corresponding to states of opposite parity on x cross, while the anticrossing occurring between the subbands of equal parity increases with decreasing L_x. For nonzero k_y all branches anticross.

Figure 3 shows the absorption spectra of the quantum wire of Fig. 1(b) for polarization vectors parallel to the x, y, and z axes (labeled x, y, and z, respectively). Broadening effects caused by sample imperfections are modeled by replacing the δ function of Eq. (1) by a Lorentzian with a full width of 2 meV at half maximum. For a polarization in the z direction only the lh parts of the Γ_8 state contribute to the absorption [Eqs. (15) or (16)]. The peak of the spectrum labeled z in Fig. 3 is mainly due to the transition $h6e1$ (from the sixth valence to the first conduction 1D subband) and partly due to nonzero k_y contribution of the transitions exhibiting lower-edge energies. For lower photon energies $\hbar\omega$ the lh contribution to the corresponding Γ_8 state is much smaller, and therefore the structures of the lower 1D absorption edges are masked by the broadening of the $h6e1$ peak.

The dependence of the absorption on the polarization in the xy plane is described by the product $J_{\mathrm{hh}1}J_{\mathrm{lh}1}\cos(2\varphi)$ of Eq. (16). The xy anisotropy is expressed by $(\alpha_x-\alpha_y)/(\alpha_x+\alpha_y)$, where α_x and α_y are the absorption coefficients for a polarization parallel to the x and y axes, respectively. If the overlap integrals $J_{\mathrm{hh}1}$ and $J_{\mathrm{lh}1}$ are of equal (opposite) sign, the absorption is weaker for x (y) polarization and the xy anisotropy is negative (positive). The magnitude of the anisotropy increases proportionally to $J_{\mathrm{hh}1}J_{\mathrm{lh}1}$ with increasing hh-lh mixing. In Fig. 3, the $h1e1$ and $h2e2$ peaks are stronger for y than for x polarization. The larger xy anisotropy at the $h2e2$ edge reflects the stronger hh-lh mixing in the second valence subband. The edge of the $h6e1$ transition located at about 53 meV exhibits the opposite polarization dependence.

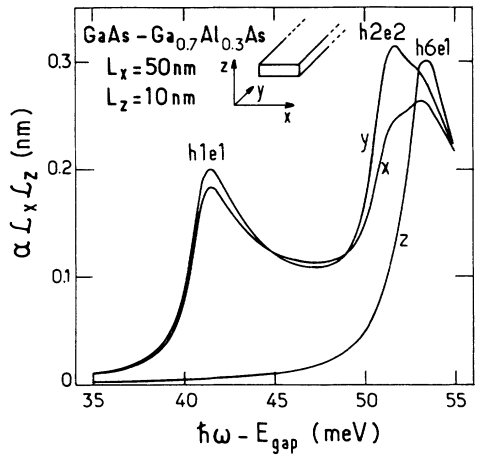

FIG. 3. Absorption of the quantum wire plotted vs photon energy $\hbar\omega$ for the three orthogonal light polarizations. E_{gap} is the band gap of bulk GaAs.

In Fig. 4 the effect of a polarization in the xy plane on the peaks of the absorption spectrum ($\hbar\omega$ equals the transition energies at $k_y=0$) is presented as a function of the wire width L_x. We have plotted the xy anisotropy for any transition that contributes substantially ($\alpha L_x L_z > 0.03$ nm) to the absorption in the energy range of the lowest 1D subband edges. Over the whole range of L_x only the $h1e1$, the $h2e2$, and the transitions involving strongly lh-like valence subbands [flat curves near the 2D lh energy E_{lh1} in Fig. 2(b)] are important. The anisotropy increases with decreasing L_x due to the increasing hh-lh mixing. At a fixed L_x, the transitions that originate from different valence subbands exhibit different magnitudes of the anisotropy. A positive (negative) xy anisotropy identifies a transition that involves a valence subband of dominant lh (hh) character.

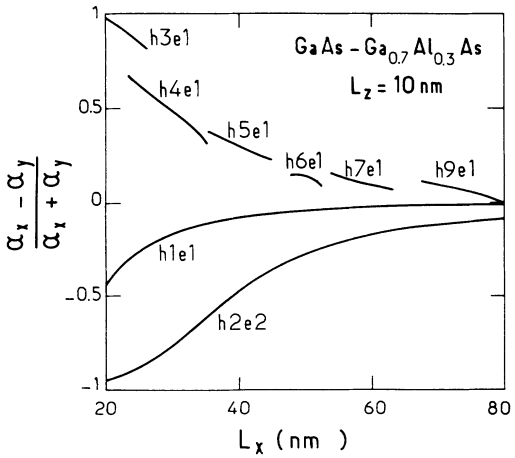

FIG. 4. xy anisotropy of the dominant 1D absorption edges as a function of the lateral wire width L_x. α_x and α_y are the absorption coefficients of the indicated transitions for a polarization parallel to the x and y axes, respectively.

The qualitative properties of the polarization-dependent absorption are independent of the model used for the lateral confinement. In Appendix B we show by an analytical perturbative treatment of the hh-lh coupling that the lateral anisotropy characterizes the hh- or lh-like character of the 1D valence subbands in the same way for any symmetric confinement potential that gives rise to spatially direct transitions.

An electric field breaks down the inversion symmetry in the direction of its application. Pointing in the z direction, it lifts the parity degeneracy in the valence band, and Eqs. (11) and (12) are no longer sufficient.

On the other hand, an electric field F in the x direction can be described by simply adding eFx to the potential V_x in Eqs. (4a) and (12). Its influence is of particular interest for real systems where charged impurities at the lateral boundaries of the quantum wire produce an electric field F along the x axis, whose magnitude may vary along the wire axis y. A simple estimate for the order of magnitude of F is the electric field in a capacitor consisting of two oppositely charged 2D sheets separated by an undoped GaAs layer of width L_x. There, a density of 10^{10} cm^{-2} of singly charged impurities results in $F \cong 1.5$ kV/cm.

The field F influences the polarization-dependent absorption in two ways. First, it shifts the edge energies of the conduction and valence subbands (Fig. 5), and with it the spectral position of the absorption peaks (Stark shift). Second, the lateral wave functions deform and separate increasingly with F. The latter effects give rise to the electric-field dependence of the xy anisotropy and to the variations of the strength of the 1D transitions plotted in Fig. 6. In the electric-field range where a given transition exhibits a sizeable strength, its transition energy and anisotropy do not change significantly. The influence of

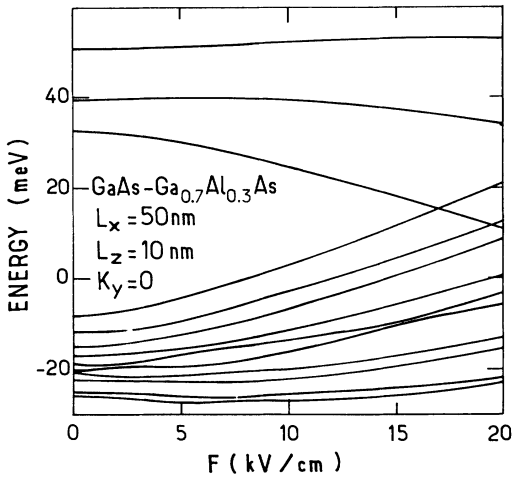

FIG. 5. Edge energies of the conduction (three topmost branches) and valence subbands of a (50×10 nm^2 cross section) quantum wire as a function of the electric field in the x direction F. The energy zero corresponds to the bottom of the conduction (top of the valence) band of bulk GaAs for the conduction (valence) subbands.

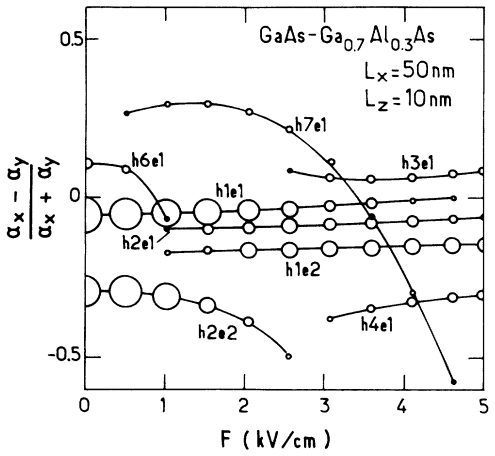

FIG. 6. Normalized xy anisotropy of the dominant ($\alpha \mathcal{L}_x \mathcal{L}_z > 0.03$ nm) absorption peaks as a function of F. The diameters of the circles indicate the strength of the peaks of the different transitions averaged over the in-plane polarization $[(\alpha_x+\alpha_y)\mathcal{L}_x\mathcal{L}_z/2]$.

spatial variations of F caused by defects in real structures can be estimated by taking the average over different spectra calculated for different F. However, for a variation of F smaller than about 2 kV/cm, the dominant spectra in this average exhibit similar polarization dependence. This indicates that the xy anisotropy is relatively stable with respect to this kind of sample imperfections. In Sec. IV the influence of randomness on the polarization spectra is studied more quantitatively.

B. Periodic lateral confinement

In a second approach we suppose a lateral confinement given by

$$V_x(x)=\pm V_1 \cos\left[\frac{2\pi}{L_x}x\right]$$

for the conduction band, and

$$V_x(x)=V_1 \cos\left[\frac{2\pi}{L_x}x\right] \tag{18}$$

for the valence band. We discuss the two different types of confinement, shown in Fig. 7. The conduction- and the valence-band edges exhibit the same absolute value of the modulation V_1 and the same periodicity L_x. The negative and positive signs in Eq. (18) correspond to the type-I and the type-II configurations, respectively. In the type-I configuration the electron and hole envelope functions are concentrated at the same positions in the x direction. This is a model for systems with a lateral modulation of the composition. For instance, the wires directly grown on a tilted GaAs substrate[6,7] exhibit a lateral modulation of the aluminum content x of the $Ga_{1-x}Al_xAs$ alloy. A confinement induced by a lateral gate pattern or modulation of the doping corresponds to

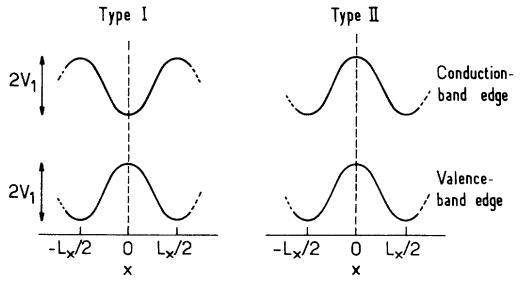

FIG. 7. The two different types of lateral confinement.

the type-II configuration (lateral surface superlattice; see, e.g., Ref. 10). It is characterized by the spatial separation of the electrons and holes into adjacent wires in the limit of a large V_1. The type-I or type-II character of 1D systems defined by etching through a 2D layer depends on the density of the charged impurities introduced at the lateral boundaries.

The lateral wave functions are written in the Bloch form

$$\varphi(x)=e^{ik_x x}\sum_K c_K e^{iKx} . \tag{19}$$

The plane-wave expansion of the periodic part extends over the vectors K of the reciprocal lattice ($K=n2\pi/L_x$; $n=\pm1,\pm2,\ldots$).

Due to the translation and inversion symmetries of Eq. (19), the whole energy dispersion can be folded in the reduced zone scheme $0\le k_x \le \pi/L_x$. The solid lines of Fig. 8 show the energies of the Γ_6 band for either $k_x=0$ or $k_x=\pi/L_x$. The dashed areas indicate the allowed minibands.

With the exception of the ground level ($k_x=0, K=0$), the energies at the edge of the reduced zone scheme are

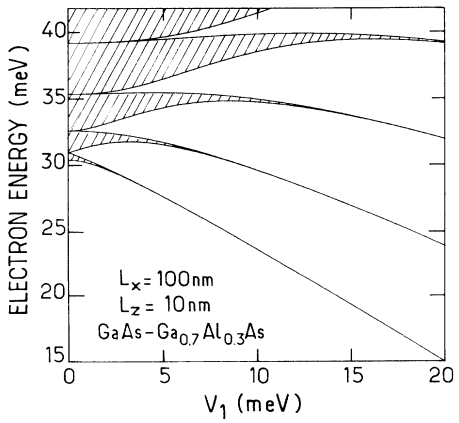

FIG. 8. Energy range covered by the miniband dispersion in k_x as a function of the strength of the periodic potential for the Γ_6 conduction band. The in-wire wave vector k_y equals zero. The energy zero is set at the bottom of the bulk GaAs conduction band.

degenerate ($K=\pm\pi/L_x$, $K=\pm 2\pi/L_x$, $K=\pm 3\pi/L_x$, . . .) at zero V_1. A periodic potential lifts these degeneracies and creates the forbidden energy regions called minigaps. The potential Eq. (18) being the first component of the Fourier expansion of a general periodic potential directly couples only the parts of Eq. (19) that differ in K by $2\pi/L_x$. First-order perturbation theory predicts a width of V_1 for the first and zero for the higher minigaps. The first minigap of Figs. 6 and 7 opens linearly in V_1 and its width equals V_1. The widths of the minigaps decrease with increasing index because an increasing order of perturbation is necessary to couple the two degenerate levels.

For large V_1, the wave functions of the lowest-energy states become strongly localized in the minima of the potential Eq. (18). The overlap of the wave functions of adjacent wires is small, as are the band widths, and the system effectively corresponds to an array of independent wires. In this limit, the relevant confinement potentials of the individual wires are nearly parabolic. For instance, the conduction-band minimum at $x=0$ can be approximated by

$$V_x(x)\cong V_1[(2\pi x/L_x)^2-1]\ . \tag{20}$$

This leads to the constant spacing of the energy levels at large V_1 in Fig. 8.

Figure 9 shows the corresponding results for the valence band. The uppermost hh-like branches show qualitatively the same behavior as the lowest electron branches. The holes localize more strongly in the lateral potential than the electrons and the bandwidths are smaller at a given V_1, since the hole effective masses in the layer plane are larger than that of the electron. The hh-lh mixing is responsible for the nonconstant spacing of the energy levels at large V_1 as well as for the intricate structure deeper in the valence band.

For the absorption we have to distinguish between type-I and type-II systems (Fig. 7). The selection rules on the envelope-function overlap are different.[26] In type-I

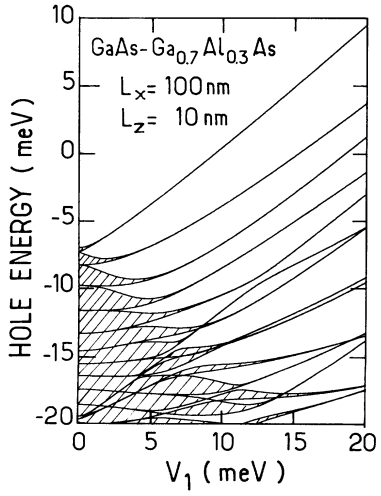

FIG. 9. Same as Fig. 8 for the Γ_8 valence band. The energy zero is set at the top of the bulk GaAs valence band.

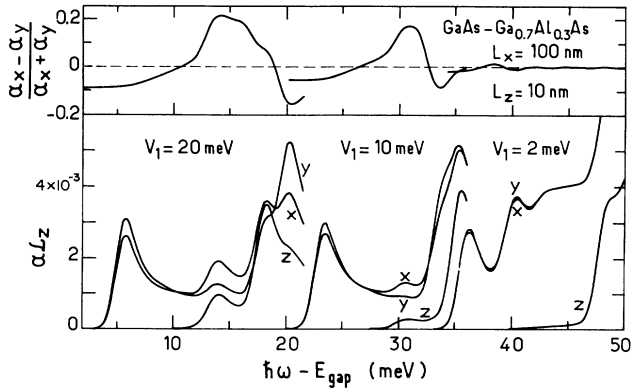

FIG. 10. Polarization-dependent absorption (lower curves) and normalized xy anisotropy (upper curves) of type-I wire arrays for different modulation V_1 of the lateral potential.

systems, transitions between electron and hole states exhibiting the same parity on x are allowed for all k_x. In type-II systems, the parity-conserving transitions being allowed at $k_x=0$ become forbidden at $k_x=\pm\pi/L_x$. In addition, transitions between states of different parity are allowed at $k_x=\pm\pi/L_x$ (forbidden at $k_x=0$). We replace the δ function of Eq. (1) by a Gaussian function with a full width of 2 meV at $1/e$ maximum.

Figure 10 shows the results for the lowest-energy transitions of the type-I system for different strengths of the lateral potential. In the lower part, the absorption for a polarization parallel to the x, y, and z axes is plotted as a function of the photon energy, while the upper part shows the normalized xy anisotropy. For $V_1=20$ meV, the peaks in the x and y absorption spectra correspond to the $h1e1$ (7 meV), $h3e1$ (14 meV), $h5e1$ (18 meV), and $h2e2$ (20 meV) transitions, respectively. The absorption spectrum shifts to higher photon energies with decreasing V_1. For small V_1, the spectra resemble the staircase shape of the 2D band-to-band absorption. In the same way as for the confinement by infinite barriers, the anisotropy of the transitions is a measure of the hh or lh character of the participating valence subband, and its amount increases with increasing lateral potential.

Figure 11 shows the results for the type-II system. The

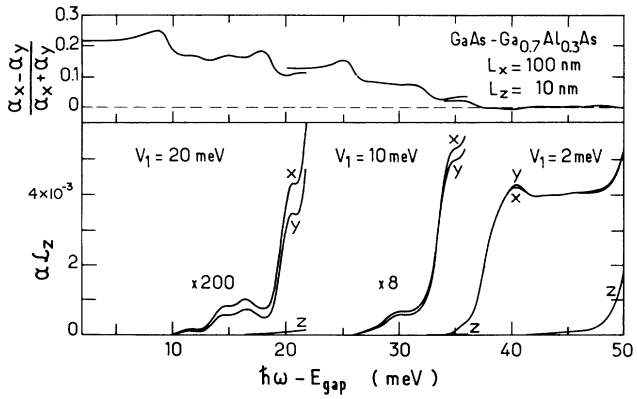

FIG. 11. Same as Fig. 10 for type-II wire arrays.

wave functions of the lowest conduction- and the topmost valence-band states are increasingly separated in space with increasing V_1. The electron-hole overlap integrals and thus the strength of the transitions increase with the photon energy $\hbar\omega$.

For type-II systems the product $J_{\mathrm{hh1}}J_{\mathrm{lh1}}$, which determines the effect of a polarization in the xy plane [Eq. (16)], depends crucially on the relative sign of the electron and hole wave function in their respective barriers. The normalized xy anisotropy increases with V_1, but there is no general connection between its sign and the hh-lh coupling, in contrast to the type-I systems.

IV. INFLUENCE OF SPATIAL FLUCTUATIONS OF THE CONFINING POTENTIAL

In the previous section, we have discussed the optical properties of different 1D systems assuming a constant shape of the lateral potential V_x over the whole structure. In practice, the shape of V_x varies from one wire to another as well as along a given one due to imperfections in the samples. The present section treats the effects of these fluctuations that are of particular importance for the comparison of the theoretical results with experiments.

We consider again the type-I wire array of Sec. III B. The lateral potential V_x is written as a sum of a target potential V^0 given by Eq. (18) and a fluctuating potential V^f:

$$V_x = V^0 + V^f ,$$

$$V^0 = V_1 \cos\left[\frac{2\pi x}{L_x}\right] , \tag{21}$$

$$V^f = \sum_{n=2}^{n_{\max}} a_n \cos\left[\frac{2\pi x}{L_x} n\right] + b_n \sin\left[\frac{2\pi x}{L_x} n\right] .$$

The Fourier expansion of V^f involving several higher components conserves the periodicity of V_x and describes a large variety of fluctuations. We define a parameter Δ for the magnitude of the deviation of V_x from V^0

$$\Delta^2 = \frac{\langle [V_x(x) - V^0(x)]^2 \rangle}{\langle V^0(x)^2 \rangle} = V_1^{-2} \sum_{n=2}^{n_{\max}} (a_n^2 + b_n^2) , \tag{22}$$

where the mean value is defined by

$$\langle f(x) \rangle = L_x^{-1} \int_{-L_x/2}^{L_x/2} f(x)\, dx .$$

The random variables a_n and b_n are initially drawn from the interval $(-1,1)$. In order to represent a random potential of given Δ, they are multiplied by a common factor c before being introduced into Eq. (21):

$$c = \Delta V_1 \left[\sum_{n=2}^{n_{\max}} (a_n^2 + b_n^2)\right]^{-1/2} .$$

The absorption spectrum of a 1D structure of deviation parameter Δ is then defined as the average over a sufficient number of spectra belonging to a different random V_x but the same Δ.

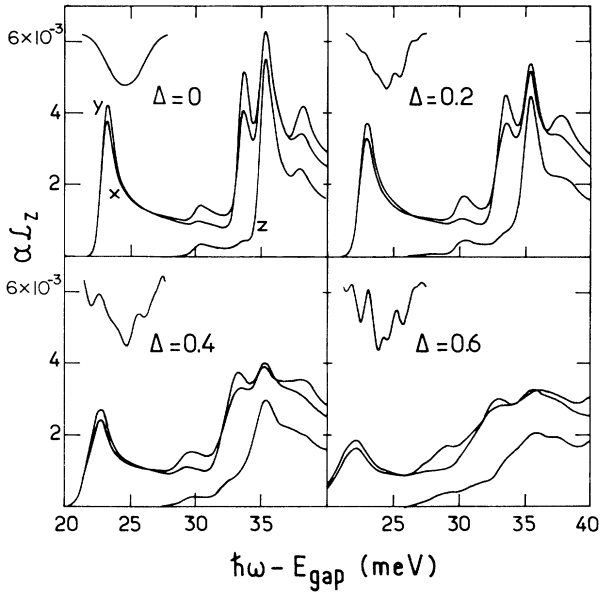

FIG. 12. Absorption spectra of a periodic type-I wire array ($L_x = 100$ nm, $V_1 = 10$ meV) for different randomness parameter Δ. The curve shown in the upper left corner of each spectrum is one example of the ensemble of random potentials corresponding to the respective Δ.

Figure 12 shows how an increasing fluctuation of V_x influences the absorption spectrum. The random potential plotted in the upper left corner of each spectrum visualizes the magnitude of the deviation corresponding to the different Δ. We use $n_{\max} = 6$. The $\Delta = 0$ spectrum of Fig. 12 describes the same physical system as the $V_1 = 10$ meV spectrum of Fig. 10, except that the width of the Gaussian function replacing the δ function of Eq. (1) is reduced by a factor of 2. With Δ increasing from 0 to 0.6 the spectrum broadens significantly. However, the broadening is similar for a polarization parallel to the x and y axes leading to a weak Δ dependence of the xy anisotropy.

Let us now look in more detail at the three dominant peaks of the spectra corresponding to the $h1e1$, $h2e2$, and $h6e1$ transitions (at 23.2, 33.7, and 35.3 meV for $\Delta = 0$), respectively. In Fig. 13 the height (solid lines) and the xy anisotropy (dashed lines) are plotted versus Δ. The peak absorption of the three transitions decreases continuously with increasing Δ. The anisotropy of the $h1e1$ transition (labeled 1) is constant in the range of the statistical uncertainty of the calculations ($\leq \pm 0.01$ for an average from 80 random spectra). This is a remarkable result in view of the strong fluctuations of V_x for large Δ.

The second hole subband is closer in energy to the 2D light hole branch and therefore exhibits a stronger hh-lh mixing than the first hole subband. This leads to the stronger xy anisotropy of the $h2e2$ (labeled 2) compared to the $h1e1$ transition at small Δ. With increasing Δ, however, the anisotropy of the $h2e2$ transition decreases, since the neighboring lh-like transitions exhibiting an opposite polarization dependence contribute increasingly to the absorption in the energy region of the $h2e2$ transi-

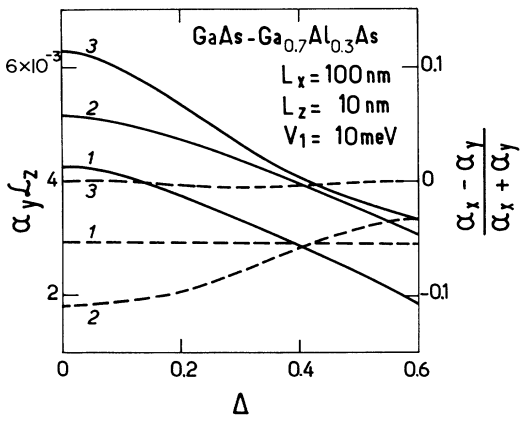

FIG. 13. Peak absorption (solid lines, left scale) and xy anisotropy (dashed lines, right scale) of the wire array of Fig. 12 as a function of Δ. The curves labeled 1, 2, and 3 correspond to $h1e1$, $h2e2$, and $h6e1$ transition peaks at 23.2, 33.7, and 35.3 meV (for $\Delta=0$), respectively.

tion. In order to prevent this decrease of the anisotropy, the separation of the transition of interest and other strong transitions exhibiting a weaker or even opposite xy anisotropy should be greater than the energy broadening. In the present case, this condition is more demanding for the $h2e2$ than for the $h1e1$ transition. The $h2e2$ transition contributes substantially to the absorption at the energy of the $h6e1$ (lh-like, labeled 3) peak. There the xy anisotropy is small even for zero Δ, since the high-energy tail is an intrinsic property of the 1D joint density of states and is not caused by broadening. A stronger lateral confinement (larger V_1 and/or smaller L_x) is needed to prevent this overlap.

V. DISCUSSION

First of all, we discuss the influence of excitonic effects neglected in the calculations. In the presence of the electron-hole Coulomb interaction the states Ψ^c and Ψ^v of Eqs. (2) and (3) are no longer the valid eigenstates. An excitonic state can be described approximately by a linear combination of direct products of Ψ^c and Ψ^v. In 2D systems this expansion can often be restricted to a sum over the electron and hole in-plane wave vectors (intrasubband couplings) because the subband separations are usually large with respect to the excitonic binding energy. In a typical 1D excitonic state the intersubband coupling (mixing of the energetically less-separated lateral subbands) has to be taken into account. A 1D excitonic transition involves an average of the band-to-band matrix elements weighed over several in-wire wave vectors k_y and lateral subband indices n_x. The singular shape of the 1D joint density of states suggests that the contributions of small k_y dominate the strength of an excitonic transition. The polarization dependence of an excitonic peak is therefore some mean value of the peak(s) of the band to band transition(s) in its energy region. In the limit of weak intersubband coupling the excitonic and the band-to-band absorption peaks should exhibit similar polarization dependence. The relative stability of the xy anisotropy (in particular of the $h1e1$ transition) with respect to variations in the confining potential demonstrated in Sec. IV supports this interpretation. Notice also that the Coulomb interaction does not alter the spatial symmetry of the problem in question.

A quantitative determination of excitonic effects on the interband absorption requires a calculation of the 1D excitonic state that includes the hh-lh mixing in the valence band. Up to now all calculations of 1D excitonic states assume simple parabolic valence subbands.[17,27,28] As already shown in Sec. II, this approximation leads to a zero xy anisotropy. The importance of excitonic effects in 1D systems is still an open question, and the experiments have to decide in which cases the band-to-band calculations describe well the physical features.

Let us finally compare our theoretical results with recent experimental findings. Tsuchiya *et al.*[6] and more recently Tanaka, Motohisa, and Sakaki[7] have measured the xy anisotropy by photoluminescence excitation spectroscopy in narrow GaAs-AlAs quantum wires directly grown on a tilted substrat. The two transitions that they observe show opposite polarization dependences that are very similar to what we calculate for the $h1e1$ and the first lh-like transitions. Both groups have explained their experimental results in the following simple approach. They evaluate the interband matrix element of the bulk semiconductor for a single wave vector $\mathbf{k}$ that is fixed in two directions by the quantum confinement and set to zero in the wire direction. However, a quantum-wire state clearly cannot be described by a single $\mathbf{k}$. At least two different (opposite) wave vectors are needed per confined direction in order to construct a standing wave.

In a quantum wire of large width ratio L_x/L_z, the dependence of the absorption on the polarization in the xy plane caused by intrinsic 1D properties is small (Fig. 4). The strong xy anisotropy observed by Kohl *et al.*[8] in etched (70×14 nm^2) GaAs-GaAlAs wires corresponds neither in sign nor in magnitude to our calculations. This may indicate that the surface corrugation of free-standing etched structures gives rise to additional electrodynamic (grating coupler, local field) effects that substantially modify the optical anisotropy, as already pointed out by the authors.

VI. CONCLUSION

In conclusion, we have presented calculations of the interband absorption in 1D structures based on an effective-mass approximation that takes the degeneracy of the valence band into account. Single wires with a lateral confinement modeled by infinite barriers and arrays of wires described by a periodic lateral potential have been studied. We have investigated two different types of the latter configuration: the spatially direct (type I) and the spatially indirect (type II) systems. While in the type-I system the absorption spectra directly reflect the change of the joint density of states from a 2D to a 1D shape, the absorption in the type-II configuration decreases strongly due to the increasing spatial separation of the electron and hole wave functions with increasing

lateral potential. In type-I systems the dependence of the absorption on the polarization in the xy plane characterizes the hh-lh mixing in the contributing valence subband. A strong xy anisotropy requires a large mixing, which can be achieved if the characteristic lengths of the confinement in the x and z directions are not too different.

We believe that our calculate polarization dependences and the underlying formalism could be a useful framework for detailed optical studies of the 1D valence-subband structures in the future. They already explain some recent experimental data.

Note added. Very recently, an effective bond-orbital model has been implemented to calculate the optical anisotropy of quantum wires and applied to the special case of the structure of Ref. 6.[29,30] This approach has led to a rough qualitative agreement with the experimental findings of Ref. 6.

ACKNOWLEDGMENTS

We would like to thank R. Ferreira for helpful discussions. We gratefully acknowledge the support from Professor G. Abstreiter and from the Deutsche Forschungs Gemeinschaft (DFG), the Centre National de la Recherche Scientifique, the Ministère de la Recherche et de la Technolgoie, and the Centre National d'Etude des Télécommunications.

APPENDIX A

In this appendix the attenuation of a light beam in 1D and 2D structures is discussed in terms of the absorption quantities defined in Sec. II A. The simplest configuration is the perpendicular penetration through a 2D (x-y) layer. The ratio of the transmitted to the incident intensities is given by

$$I_t/I_i=(1-\alpha\mathcal{L}_z)\ . \tag{A1}$$

For a propagation parallel to the 2D plane (for instance, in the y direction), the intensity profile of the light beam $I(z)$ is of importance. We define an effective beam width in the z direction by

$$\tilde{L}_z=\int dz\, I(z)/I_0\ , \tag{A2}$$

where I_0 stands for the intensity in the interior of the active structure. For the attenuation of the beam we obtain

$$I(y)=I(0)e^{-\alpha\mathcal{L}_z y/\tilde{L}_z}\ . \tag{A3}$$

In the following we will treat the 1D structure (wire axis in the y direction) in a very similar way. For a beam that penetrates perpendicular through the wire (propagation parallel to x) we get

$$I_t/I_i=(1-\alpha\mathcal{L}_x\mathcal{L}_z/\tilde{L}_z)\ . \tag{A4}$$

For a propagation parallel to z, the parameter $\tilde{L}_z$ has to be replaced by $\tilde{L}_x$ [defined by the equivalent of Eq. (A2) for the x direction].

A light beam that propagates parallel to the wire axis is described by

$$I(y)=I(0)e^{-\alpha\mathcal{L}_x\mathcal{L}_z y/\tilde{S}_{x,z}}\ , \tag{A5}$$

where $\tilde{S}_{x,z}$ is related to the intensity profile $I(x,z)$ of the beam by

$$\tilde{S}_{x,z}=\int dx\int dz\, I(x,z)/I_0\ . \tag{A6}$$

In all these configurations the attenuation is described by two well-defined, independent quantities that represents the absorption properties ($\alpha\mathcal{L}_z$ for 2D and $\alpha\mathcal{L}_x\mathcal{L}_z$ for 1D structures) on the one hand, and the respective intensity profiles of the light wave ($\tilde{L}_x,\tilde{L}_z,\tilde{S}_{x,z}$) on the other hand.

APPENDIX B

In this appendix we treat the hh-lh coupling by perturbation theory and derive analytically the sign of the factor $J_{\mathrm{hh1}}J_{\mathrm{lh1}}$ that determines the effect of a lateral polarization via Eq. (16). Since we are interested in the peaks of the 1D joint density of states, we set k_y to zero.

Let us now look at interband transitions to a given 1D conduction-band state. When the confinement potential in the x direction has a similar shape for the holes as for the electrons (type-I systems, see Fig. 7), only the lateral valence-band wave functions with the same subband index as the final conduction-band state in question contribute significantly to the electron-hole overlap integrals. These lateral functions are labeled $\varphi_{\mathrm{hh}}(x)$ for the heavy and $\varphi_{\mathrm{lh}}(x)$ for the light hole.

To zeroth order of perturbation (in the absence of hh-lh coupling), the valence-band eigenfunctions are either hh states

$$|\Psi_{\mathrm{hh}}\rangle_0=\begin{pmatrix}\varphi_{\mathrm{hh}}(x)\\0\end{pmatrix} \tag{B1}$$

or lh states

$$|\Psi_{\mathrm{lh}}\rangle_0=\begin{pmatrix}0\\\varphi_{\mathrm{lh}}(x)\end{pmatrix}\ . \tag{B2}$$

The two-component vectors in Eqs. (B1) and (B2) operate on the basis $[\chi_{\mathrm{hh1}}(z)u^{v}_{3/2},\ \chi_{\mathrm{lh1}}(z)u^{v}_{-1/2}]$ and $[\chi_{\mathrm{hh1}}(z)u^{v}_{-3/2},\ \chi_{\mathrm{lh1}}(z)u^{v}_{1/2}]$ for the solutions $\Psi\uparrow$ and $\Psi\downarrow$ [Eq. (11)], respectively.

To first order in the off-diagonal terms of H of Eq. (12), the pure hh state [Eq. (B1)] gets a lh contribution [from Eq. (B2)] and vice versa:

$$|\Psi_{\mathrm{hh}}\rangle_1=|\Psi_{\mathrm{hh}}\rangle_0+c\,|\Psi_{\mathrm{lh}}\rangle_0\ , \tag{B3}$$

$$|\Psi_{\mathrm{lh}}\rangle_1=|\Psi_{\mathrm{lh}}\rangle_0-c\,|\Psi_{\mathrm{hh}}\rangle_0\ , \tag{B4}$$

$$c=\frac{\hbar^2}{2\mu}\frac{\int dx\,\varphi_{\mathrm{lh}}(x)(-\partial_x^2)\varphi_{\mathrm{hh}}(x)}{E^0_{\mathrm{hh}}-E^0_{\mathrm{lh}}}$$

$$=\frac{\hbar^2}{2\mu}\frac{\int dx\,\varphi'_{\mathrm{lh}}(x)\varphi'_{\mathrm{hh}}(x)}{E^0_{\mathrm{hh}}-E^0_{\mathrm{lh}}}>0\ . \tag{B5}$$

For a stronger confinement in the z than in the x direc-

tion, the difference between the zeroth-order hh and lh energies ($E^0_{hh}-E^0_{lh}$) is positive for the uppermost valence subbands. The integral in the numerator of Eq. (B5) is positive as well, since $\varphi_{hh}(x)$ and $\varphi_{lh}(x)$ have similar shape. The resulting positive sign of c implies a positive (negative) factor $J_{hh1}J_{lh1}$ for an interband transition involving the state $|\varphi_{hh}\rangle_1$ ($|\varphi_{lh}\rangle_1$). Together with Eq. (16) it follows that

$$\frac{\alpha_x-\alpha_y}{\alpha_x+\alpha_y}>0 \quad \text{for } |\Psi_{lh}\rangle_1 ,$$
$$\frac{\alpha_x-\alpha_y}{\alpha_x+\alpha_y}<0 \text{ for } |\Psi_{hh}\rangle_1 . \tag{B6}$$

[1]See, e.g., S.P. Beaumont, in *Proceedings of the NATO-ASI "Granular Nanoelectronics," II Ciocco, Italy, 1990,* edited by D. K. Ferry, J. R. Barker, and C. Jacoboni (Plenum, New York, in press), Vol. 25.

[2]J. Cibert, P. M. Petroff, G. J. Dolan, S. J. Pearton, A. C. Gossard, and J. H. English, Appl. Phys. Lett. **49**, 1275 (1986).

[3]Y. Hirayama, S. Tarucha, Y. Suzuki, and H. Okamoto, Phys. Rev. B **37**, 2774 (1988).

[4]D. Gershoni, H. Temkin, G. J. Dolan, J. Dunsmuir, S. N. G. Chu, and M. B. Panish, Appl. Phys. Lett. **53**, 995 (1988).

[5]E. Kapon, S. Simhony, R. Bhat, and D. M. Hwang, Appl. Phys. Lett. **55**, 2715 (1989).

[6]M. Tsuchiya, J. M. Gaines, R. H. Yan, R. J. Simes, P. O. Holtz, L. A. Coldren, and P. M. Petroff, Phys. Rev. Lett. **62**, 466 (1989).

[7]M. Tanaka, J. Motohisa, and H. Sakaki, Surf. Sci. **228**, 408 (1990).

[8]M. Kohl, D. Heitmann, P. Grambow, and K. Ploog, Phys. Rev. Lett. **63**, 2124 (1989).

[9]M. Kohl, D. Heitmann, W. W. Rühle, P. Grambow, and K. Ploog, Phys. Rev. B **41**, 12 338 (1990).

[10]J. S. Weiner, G. Danan, A. Pinczuk, J. Valladares, L. N. Pfeiffer, and K. West, Phys. Rev. Lett. **63**, 1641 (1989).

[11]T. Egeler, G. Abstreiter, G. Weimann, T. Demel, D. Heitmann, P. Grambow, and W. Schlapp, Phys. Rev. Lett. **65**, 1804 (1990).

[12]J. A. Brum and G. Bastard, Superlatt. Microstruct. **4**, 443 (1988).

[13]M. Sweeny, J. Xu, and M. Shur, Superlatt. Microstruct. **4**, 623 (1988).

[14]D. S. Citrin and Y. C. Chang, Phys. Rev. B **40**, 5507 (1989); J. Appl. Phys. **68**, 161 (1990).

[15]P. C. Sercel and K. J. Vahala, Phys. Rev. B **42**, 3690 (1990).

[16]M. Asada, Y. Miyamoto, and Y. Suematsu, Jpn. J. Appl. Phys. **24**, L95 (1985).

[17]J. W. Brown and H. N. Spector, Phys. Rev. B **35**, 3009 (1987).

[18]D. A. B. Miller, D. S. Chemla, and S. Schmitt-Rink, Appl. Phys. Lett. **52**, 2154 (1988).

[19]U. Bockelmann and G. Bastard, Europhys. Lett. **15**, 215 (1991).

[20]E. O. Kane, J. Phys. Chem. Solids **1**, 249 (1957).

[21]G. Bastard, *Wave Mechanics Applied to Semiconductor Heterostructures* (Les Editions de Physique, Les Ulis, France, 1988).

[22]J. M. Luttinger and W. Kohn, Phys. Rev. **97**, 869 (1955).

[23]J. M. Luttinger, Phys. Rev. **102**, 1030 (1956).

[24]M. Altarelli, in *Semiconductor Superlattices and Heterojunctions,* edited by G. Allan, G. Bastard, N. Boccara, M. Lannoo, and M. Voos (Springer-Verlag, Berlin, 1986).

[25]R. Ferreira and G. Bastard, Phys. Rev. B **43**, 9687 (1991).

[26]P. Voisin, G. Bastard, and M. Voos, Phys. Rev. B **29**, 935 (1984).

[27]M. H. Degani and O. Hipolito, Phys. Rev. B **35**, 9345 (1987).

[28]A. D'Andrea and R. Del Sole, Solid State Commun. **74**, 1121 (1990).

[29]D. S. Citrin and Y. C. Chang, J. Appl. Phys. **69**, 2685 (1991).

[30]D. S. Citrin and Y. C. Chang, Phys. Rev. B **43**, 11 703 (1991).